

Long-term dynamical evolution of dusty ejecta from Deimos

Martin Makuch*, Alexander V. Krivov, Frank Spahn

Institute of Physics, Nonlinear Dynamics Group, University of Potsdam, Am Neuen Palais 10, Bldg. 19, 14469 Potsdam, Germany

Received 2 June 2004; received in revised form 2 September 2004; accepted 16 September 2004

Available online 22 December 2004

Abstract

We re-assess expected properties of the presumed dust belt of Mars formed by impact ejecta from Deimos. Previous studies have shown that dynamics of Deimos particles are dominated by two perturbing forces: radiation pressure (RP) and Mars' oblateness (J2). At the same time, they have demonstrated that lifetimes of particles, especially of grains about ten of micrometers in size, may reach more than 10^4 years. On such timescales, the Poynting–Robertson drag (PR) becomes important. Here we provide a study of the dynamics under the combined action of all three perturbing forces. We show that a PR decay of the semimajor axes leads to an adiabatic decrease of amplitudes and periods of oscillations in orbital inclinations predicted in the framework of the underlying RP+J2 problem. Furthermore, we show that smallest of the long-lived Deimos grains (radius $\approx 5\text{--}10\ \mu\text{m}$) may reach a chaotic regime, resulting in unpredictable and abrupt changes of their dynamics. The particles just above that size ($\approx 10\text{--}15\ \mu\text{m}$) should be the most abundant in the Deimos torus. Our dynamical analysis, combined with a more accurate study of the particle lifetimes, provides corrections to earlier predictions about the dimensions and geometry of the Deimos torus. In addition to a population, appreciably inclined and shifted towards the Sun, the torus should contain a more contracted, less asymmetric, and less tilted component between the orbits of Phobos and Deimos.

© 2004 Elsevier Ltd. All rights reserved.

PACS: 96.30.Gc; 94.10.Nh; 96.30.Wr

Keywords: Mars; Deimos; Ejecta; Dynamics; Radiation pressure; Poynting–Robertson drag

1. Introduction

Like all bodies in the Solar system, the tiny Martian moons Phobos and Deimos are continuously bombarded by interplanetary micrometeoroids. Due to these hypervelocity impacts secondary material is ejected from the surface of the bodies. The mass of the ejecta is several orders of magnitude greater than the mass of projectiles. The velocities of the ejected debris are typically tens of meters per second, which is comparable with, or greater than, the escape velocity from the satellite surface. Escaping particles should generate

ethereal dust tori along the orbits of the parent satellites (first suggested by Soter, 1971). These putative dust tori, which still escape direct detection (see Showalter et al., 2001, for the most recent attempt), were theoretically studied by many authors (see Krivov and Hamilton, 1997 for detail overview of previous work).

The dynamics of the ejecta are very complex, being controlled by a large array of perturbing forces. These include gravity of the oblate Mars, solar radiation pressure, Lorentz force, and others. Relative importance of a particular perturbation depends mainly on the size of the grains and their position in the Martian system. As the ejecta dynamics depend on the grain size, different-sized ejecta of both moons form several populations with quite distinct properties. Using the terminology of Krivov (1996), Population 0 consists of

*Corresponding author. Tel.: +49 331 9771 390; fax: +49 331 9771 142.

E-mail address: makuch@agnld.uni-potsdam.de (M. Makuch).

the largest grains with radii $\gtrsim 1$ mm. Since non-gravitational perturbations on the macroscopic grains are weak, they stay within confined tori along the moons' orbits, the size of which is determined by the initial ejection velocity distribution (Kholshchevnikov et al., 1993). As these particles rapidly re-accrete on the parent moon, their lifetimes and related number densities are very low. Population I contains smaller particles with radii from hundreds down to tens of microns and lifetimes between tens of years (Phobos) and *tens of thousands of years* (Deimos). These should form extended asymmetric tori and represent the dominant component of the entire dust complex. Their major loss mechanism is still re-accretion by the parent moon. Combined influence of the solar radiation pressure and Mars oblateness causes periodic oscillations of eccentricity and inclination. Below a certain critical radius s_{crit} ($\sim 10 \mu\text{m}$, see Krivov et al., 1996), the amplitude of the eccentricity oscillations becomes so high that the particles collide with Mars at the pericenter of their orbits in less than 1 year, so they are present with low number densities. These grains are classified as Population II. Tiniest, submicron-sized fragments (Population III) are strongly influenced by electromagnetic forces and solar wind. They are swiftly swept out from the vicinity of Mars in 10–100 days and form an extended, highly variable halo around Martian system (Horányi et al., 1990, 1991). However, a small fraction of the submicron-sized grains ejected from Martian moons at larger speeds can reach stable orbits transverse to the ecliptic plane with lifetimes exceeding 1000 years (Howard et al., 2003).

The aim of this work is to analyse long-term dynamical evolution of the Deimos particles of Population I, which are expected to dominate the dust environment at Mars (Juhász and Horányi, 1995). The dynamics of grains governed by two strongest perturbations, solar radiation pressure (RP) and planetary oblateness (J2), were studied both analytically and numerically in detail before (Krivov et al., 1996; Hamilton, 1996; Ishimoto, 1996; Krivov and Hamilton, 1997). However, the Poynting–Robertson effect (PR), which becomes important over extremely long lifetimes of tens of thousands of years, has never been included in previous models of dust at Mars. This paper provides a study of the dynamics under the combined influence of all three perturbing forces: RP, J2, and PR.

Section 2 discusses equations of motion, which are then used in Section 3 to study the dynamical evolution of different-sized ejecta from Deimos. Section 4 focuses on lifetimes of the grains in Martian system. The results are used in Section 5 to find out the expected structure of the Deimos torus and to compare it with the Phobos one. Section 6 lists our conclusions.

2. Equations of motion

2.1. Equations of motion in coordinates

The most straightforward way to study the dynamics is numerical integration of the equation of motion of a particle under the influence of all three perturbing forces:

$$m\ddot{\vec{r}} = \vec{F}_{\text{GR}} + \vec{F}_{\text{J2}} + \vec{F}_{\text{RP}} + \vec{F}_{\text{PR}}, \quad (1)$$

where the right-hand side terms represent the gravitational force of the spherical Mars \vec{F}_{GR} , oblateness of the planet \vec{F}_{J2} , direct radiation pressure \vec{F}_{RP} and Poynting–Robertson drag \vec{F}_{PR} . We used a code based on the Everhart's (1985) method with the automatic choice of step size. The integration interval was chosen in very broad range from $\sim 10^3$ up to $\sim 10^5$ Martian years (1.88 years; henceforth denoted by [M.y.]) depending on conditions and purpose of the simulation. The design of our integration code allows us to follow a set of trajectories with different initial data, which can be chosen with a large degree of flexibility.

2.2. Orbit-averaged equations in orbital elements

Since we are interested in long-term dynamics, direct numerical integrations described above would imply very long computing times. An alternative would be to numerically integrate orbit-averaged equations of motion in orbital elements, which we describe in this section.

We start with a brief description of the PR effect. The PR force \vec{F}_{PR} is a component of the radiation pressure force and is usually treated separately from the direct radiation pressure \vec{F}_{RP} . Since it is a dissipative force, acting in opposite direction to the particle velocity, the grains gradually lose orbital energy and angular momentum. This results in a decrease of semimajor axis a with time which, in the orbit-averaged approximation, is given by (Burns et al., 1979):

$$\frac{\dot{a}}{a} = Dn_{\odot} \quad (2)$$

with

$$D = \frac{3}{8} \left(\frac{1}{n_{\odot}} \right) \left(\frac{S_0}{R_M^2} \right) \left(\frac{Q_{\text{pr}}}{c^2 \rho s} \right) (5 + \cos^2 i). \quad (3)$$

Here, $S_0 = 1.36 \times 10^6 \text{ erg cm}^{-2}$ is the solar constant, R_M the heliocentric distance of Mars in AU, n_{\odot} the mean motion of Sun, i the inclination of the particle orbit, c the speed of light, ρ and s are density and radius of the particle. Q_{pr} is the radiation pressure efficiency factor depending on the grain radius s . Replacing $\cos^2 i$ with unity, Eq. (2) implies an exponential decay of the semimajor axis: $a = a_0 \exp(-Dn_{\odot}t)$, where a_0 is the initial semimajor axis.

In the orbit-averaged approximation, the PR force does not affect the eccentricity of a planetocentric orbit (Burns et al., 1979)—in contrast to heliocentric motion, which circularises under the action of PR. The changes in other orbital elements are small and can be ignored.

Following Krivov et al. (1996) we express the equations of motion of a particle in terms of Lagrange elements h, k, p, q , defined as

$$\begin{aligned} h &= e \cos \tilde{\omega}, & k &= e \sin \tilde{\omega}, \\ p &= \sin i \cos \Omega, & q &= \sin i \sin \Omega, \end{aligned} \quad (4)$$

where $\tilde{\omega} \equiv \Omega + g$ is the longitude of pericenter and e, Ω, g are eccentricity, longitude of node and argument of pericenter, respectively. As an independent variable, we use the longitude of the Sun λ_{\odot} , which makes the equations of motion dimensionless. Neglecting the eccentricity of Martian orbit, λ_{\odot} is a linear function of time:

$$\lambda_{\odot} = \lambda_{\odot 0} + n_{\odot} t, \quad (5)$$

where $\lambda_{\odot 0}$ is the initial solar longitude at the moment of ejection ($t = 0$) or, more exactly, when a particle reaches the boundary of the moon's action sphere.

The orbit-averaged equations of motion under RP and J2 were derived by Krivov et al. (1996). They can be generalised to include the PR effect by adding Eq. (2), rewritten in the same variables. The resulting system reads:

$$\frac{da}{d\lambda_{\odot}} = -Da, \quad (6)$$

$$\begin{aligned} \frac{dh}{d\lambda_{\odot}} &= -k\omega \frac{5I^2 - 2I - 1}{2E^4} \\ &\quad - \frac{C}{E(1+I)} \{ [p - Hh]q \cos \lambda_{\odot} \\ &\quad + [E^2(1+I) - p(p - Hh)] \cos \varepsilon \sin \lambda_{\odot} \\ &\quad + [E^2(1+I)p - IKk] \sin \varepsilon \sin \lambda_{\odot} \}, \end{aligned} \quad (7)$$

$$\begin{aligned} \frac{dk}{d\lambda_{\odot}} &= h\omega \frac{5I^2 - 2I - 1}{2E^4} \\ &\quad + \frac{C}{E(1+I)} \{ [q - Hk]p \cos \varepsilon \sin \lambda_{\odot} \\ &\quad + [E^2(1+I) - q(q - Hk)] \cos \lambda_{\odot} \\ &\quad - [E^2(1+I)q - IKh] \sin \varepsilon \sin \lambda_{\odot} \}, \end{aligned} \quad (8)$$

$$\begin{aligned} \frac{dp}{d\lambda_{\odot}} &= q\omega \frac{I}{E^4} + \frac{C}{E(1+I)} [Hp - (1+I)h] \\ &\quad \times [(p \cos \varepsilon - I \sin \varepsilon) \sin \lambda_{\odot} - q \cos \lambda_{\odot}], \end{aligned} \quad (9)$$

$$\begin{aligned} \frac{dq}{d\lambda_{\odot}} &= -p\omega \frac{I}{E^4} + \frac{C}{E(1+I)} [Hq - (1+I)k] \\ &\quad \times [(p \cos \varepsilon - I \sin \varepsilon) \sin \lambda_{\odot} - q \cos \lambda_{\odot}], \end{aligned} \quad (10)$$

with

$$\begin{aligned} E &= \sqrt{1 - e^2} = \sqrt{1 - h^2 - k^2}, \\ I &= \cos i = \sqrt{1 - p^2 - q^2}, \\ H &= hp + kq, \\ K &= hq - kp, \end{aligned} \quad (11)$$

where ε denotes the obliquity of Mars (25°), and C and ω are dimensionless parameters that characterise the strength of the radiation pressure and oblateness (see Krivov et al., 1996, for an exact definition).

Eqs. (6)–(11) are coupled through the parameters D, C and ω . The first of them has a weak dependence on the inclination i (see Eq. (3)), which we take into account in numerical integrations. The other parameters, C and ω , are functions of semimajor axis:

$$C(a) = C_0 \left(\frac{a}{a_0} \right)^{1/2}, \quad \omega(a) = \omega_0 \left(\frac{a}{a_0} \right)^{-7/2}, \quad (12)$$

where $C_0 \equiv C(a_0)$ and $\omega_0 \equiv \omega_0(a_0)$. Assuming a grain density of $\varrho = 2.37 \text{ g cm}^{-3}$, C_0 and ω_0 can be expressed as

$$\begin{aligned} C_0 &= 4.10 \frac{Q_{\text{pr}}(s)}{s[\mu\text{m}]} \text{ (Phobos' ejecta)}, \\ C_0 &= 6.49 \frac{Q_{\text{pr}}(s)}{s[\mu\text{m}]} \text{ (Deimos' ejecta)} \end{aligned} \quad (13)$$

and

$$\begin{aligned} \omega_0 &= 0.829 \text{ (Phobos' ejecta)}, \\ \omega_0 &= 0.0335 \text{ (Deimos' ejecta)}. \end{aligned} \quad (14)$$

Like equations in coordinates (1), the equations in elements, Eqs. (6)–(11), were integrated by the Everhart routine with the automatic choice of step size. Since these integrations are by about two orders of magnitude faster, we use them as the main tool to study the dynamics in this paper. Of course, the results were thoroughly tested against those coming from Eqs. (1). Examples of that comparison will be given in subsequent sections.

3. Grain dynamics

Before we pass on to a discussion of the particle dynamics, we shall specify the dependence of the radiation pressure forces on the particle sizes. Throughout the paper, we use compact spherical grains made of one of the silicates, a dielectric material with less absorption in visible light (for its parameters, see Kimura et al., 1997; Krivov et al., 1998). The radiation pressure efficiency Q_{pr} as a function of particle's radius is given in Table 1. The bulk density of this material is $\varrho = 2.37 \text{ g cm}^{-3}$. We note that, since grains with the same ratio of $Q_{\text{pr}}/(s\varrho)$ experience the same acceleration by radiation pressure, the results can be easily scaled to

different values of the radiation pressure factor Q_{pr} and material density ρ . As an example, an $8\ \mu\text{m}$ grain ($Q_{\text{pr}} = 0.41$, $\rho = 2.37\ \text{g cm}^{-3}$) in this paper corresponds to a $23\ \mu\text{m}$ grain in Krivov et al. (1996) who adopted $Q_{\text{pr}} = 1$ and $\rho = 2\ \text{g cm}^{-3}$.

3.1. Radiation pressure alone

On timescales up to hundreds of years, i.e. before the semimajor axes of the Deimos ejecta have been lowered by the PR effect considerably, their dynamics are dominated by radiation pressure (e.g., Krivov et al., 1996; Hamilton and Krivov, 1996). It causes the orbital eccentricity to oscillate with a period close to 1 M.y. and an amplitude depending on the radiation pressure strength:

$$e_{\text{max}} = 2C/(1 + C^2), \quad (15)$$

provided that the obliquity ε is small. The inclination experiences periodic changes of a longer period (tens of M.y. for $\sim 10\ \mu\text{m}$ particles), with both period and

Table 1
Radiation pressure efficiency of the material adopted in the calculations of the radiation pressure force

$s[\mu\text{m}]$	5	6	7	8	10	15	20	30
Q_{pr}	0.442	0.433	0.426	0.411	0.400	0.385	0.378	0.374

amplitude depending on C and hence on the grain size. This is illustrated by Fig. 1 that depicts the evolution of both orbital elements for Deimos particles with two specific radii, 15 and $7.5\ \mu\text{m}$. Plotted are results obtained by both methods described in previous sections: integration of orbit-averaged equations in Lagrangian elements (Eqs. (6)–(11), lines) and, for comparison, by direct numerical integration of the equations in coordinates (Eq. (1), points). The plots show that Eqs. (6)–(11) provide an excellent accuracy.

The eccentricity panels in Fig. 1 also reveal a slight modulation of the eccentricity oscillation by the variation of the inclination. This second period in the eccentricity is equal to the “main” period in the inclination (about 20 M.y. for $s = 15\ \mu\text{m}$ and 8 M.y. for $s = 7.5\ \mu\text{m}$). The amplitude is about one or two percent of e_{max} .

Eq. (15) determines the critical value of C , and therefore of the particle size, for which $e_{\text{max}} = 1 - R/a_0 = 0.855$ (R is the Mars radius) and the pericenter of orbit reaches the Mars surface. Eqs. (15) and (13) yield $s_{\text{crit}} \approx 5\ \mu\text{m}$. With test numerical integrations of (1), in which we included additional forces and effects (ellipticity of Mars’ orbit, planetary shadow), we checked that the “realistic” critical size is somewhat larger, $\approx 7\ \mu\text{m}$. Since smaller particles are produced at the moon surface at higher rates than

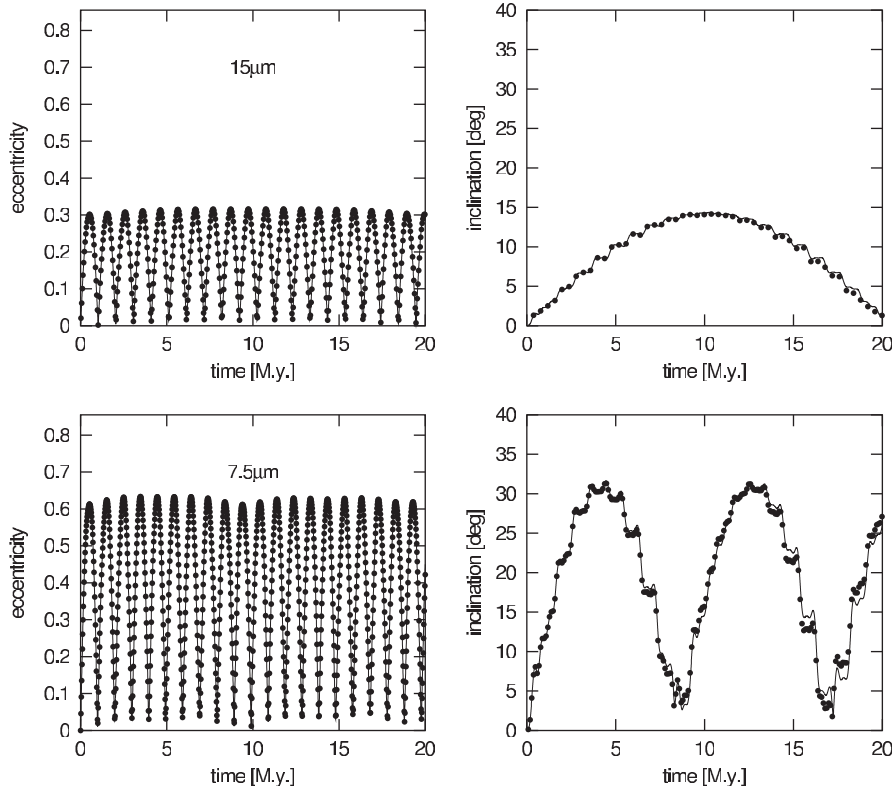


Fig. 1. Dynamical evolution of $15\ \mu\text{m}$ (top) and $7.5\ \mu\text{m}$ Deimos ejecta (bottom) under the radiation pressure. Points: integrations of Eq. (1), solid lines: integrations of Eqs. (6)–(11). Left: eccentricity, right: inclination. The upper edge of the eccentricity panels corresponds to the critical eccentricity 0.855, for which the pericenters of orbits touch the Martian surface.

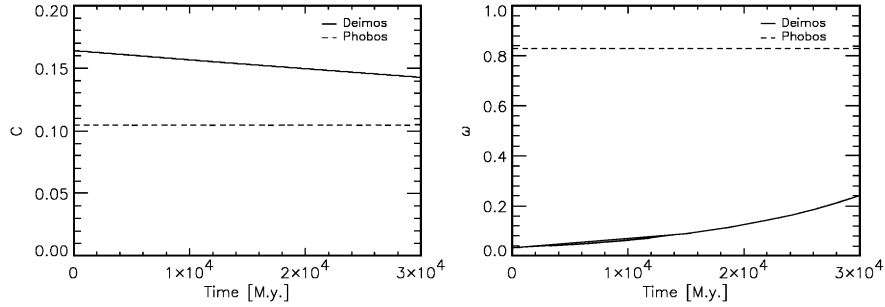


Fig. 2. Time evolution of the radiative (C) and oblateness (ω) parameters for a $15\ \mu\text{m}$ Deimos particle. Horizontal dashed lines are the parameters of a like-sized Phobos grain.

larger ones, grains just above this critical size are expected to dominate the Population I. This explains the “working range” of sizes considered in this paper: from $\approx 7\ \mu\text{m}$ to $\approx 30\ \mu\text{m}$.

3.2. Radiation pressure and planetary oblateness

A more accurate description of the dynamics can be achieved by taking into account the oblateness of Mars, parameterised by the force parameter ω . From the system of Eqs. (7)–(11), neglecting the terms of order e^2 , i^2 and $\sin i$ and assuming that ω is small, Krivov et al. (1996) found approximate analytic expressions for the periods of oscillation of e and i and their amplitudes. The amplitude and period of oscillations of eccentricity are

$$e_{\max} \approx \frac{2C(\cos \varepsilon + \omega)}{1 - \omega^2}, \quad (16)$$

$$T_e \approx 1/(1 - \omega). \quad (17)$$

The amplitude and period of oscillations of the inclination are

$$i_{\max} \approx \arcsin \frac{2d}{v}, \quad (18)$$

$$T_i \approx \frac{1}{v}, \quad (19)$$

where

$$d = \frac{C^2}{2} \frac{1 + \omega \cos \varepsilon}{1 - \omega^2} \sin \varepsilon \quad \text{and} \quad (20)$$

$$v = \omega + \frac{C^2 \cos \varepsilon + \omega}{2(1 - \omega^2)}.$$

3.3. Radiation pressure, planetary oblateness and Poynting–Robertson drag

We now add the PR force into the model. With the PR effect at work, a decrease of the semimajor axis makes “constants” C and ω (Eq. (12)) functions of time. The time evolution of C and ω for a $15\ \mu\text{m}$ Deimos particle is depicted in Fig. 2. Using then (16)–(17) and

(18)–(19), we calculated the long-term time evolution of the amplitudes and periods of oscillations in eccentricity and inclination (Fig. 3, lines). While for eccentricity the amplitude and period stay nearly constant, for inclination both quantities experience a moderate decrease with time. This falls in a qualitative agreement with numerical integrations of Eqs. (6)–(11) (Fig. 3, points). A quantitative agreement is good for all quantities except for i_{\max} . The discrepancy is caused by simplifying assumptions made by Krivov et al. (1996) in their derivation of Eq. (18). Note that another analytic formula for i_{\max} obtained by Hamilton (1996) (his $2i_{\text{forced}}$) gives nearly the same result as Eq. (18).

Closer to Mars the radiation pressure parameter C decreases and the oblateness parameter ω increases. Thus, both perturbing forces become simultaneously important for the dynamics of particles. This is the case for ejecta from Phobos, which makes their dynamics much more complicated (e.g., Krivov et al., 1996; Ishimoto, 1996; Hamilton, 1996; Hamilton and Krivov, 1996). One of the central ideas of this study is that the inclusion of the PR dissipation causes the Deimos particles to gradually migrate inward. Consequently, we expect that, after sufficient time, the Deimos particles switch into the “Phobos regime”. Accordingly, in the subsequent sections, we follow the orbital evolution of the Deimos particles over time spans long enough for the orbits to shrink appreciably.

3.4. Gradual orbit modifications

Numerical integration of orbit-averaged 3D equations of motion (6)–(11) performed with zero initial eccentricities and inclinations over longer timescales gives the results shown in Fig. 4. Panels illustrate the time evolution of the semimajor axis, eccentricity and inclination of the same particles as in Fig. 1: with radii $15\ \mu\text{m}$ (left) and $7.5\ \mu\text{m}$ (right) ejected from Deimos in Martian autumn equinox ($\lambda_{\odot} = 180^\circ$). In Fig. 4 (top) the decrease of semimajor axis can be easily recognised. As expected from analytic estimates (see Fig. 3), the amplitude of the eccentricity oscillations stays nearly

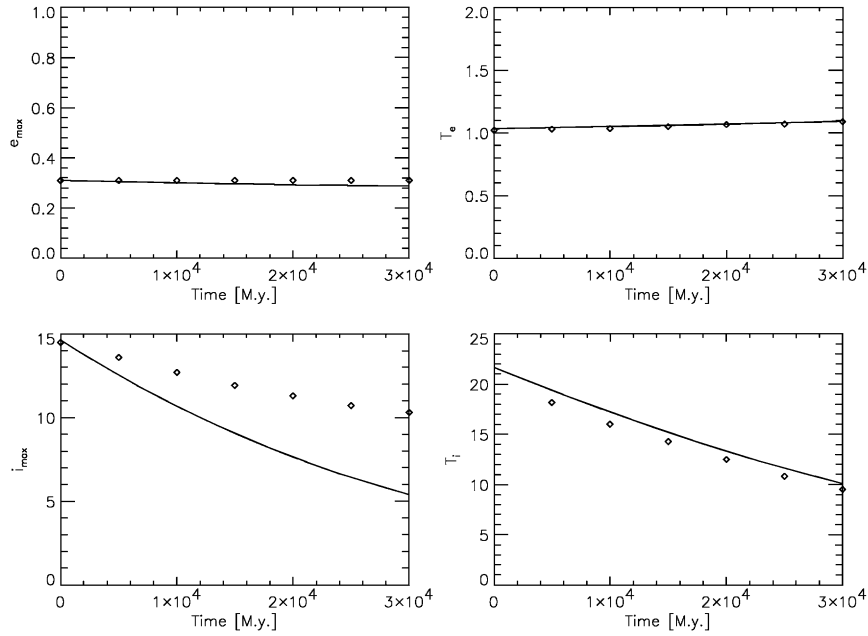


Fig. 3. Time evolution of the amplitude and period of eccentricity and inclination of the 15 μm Deimos ejecta.

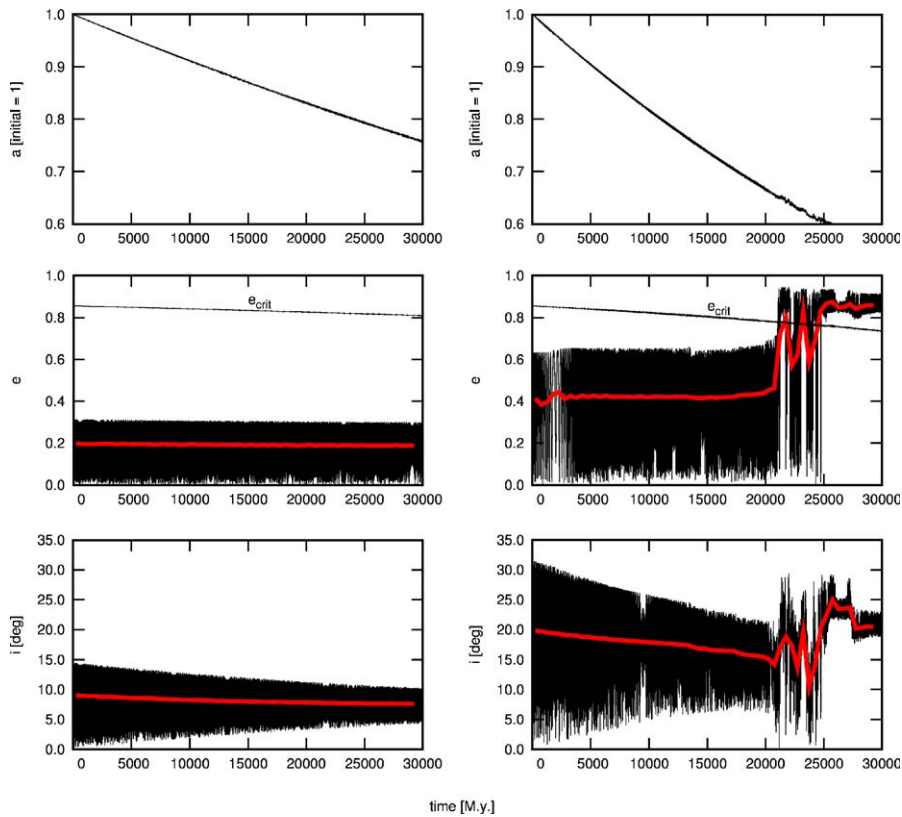


Fig. 4. Time evolution of orbital elements of 15 μm (left) and 7.5 μm (right) grains ejected into the circular Deimos orbit under the influence of radiation pressure, oblateness of Mars, and the PR effect. The curves were obtained by numerical integration of Eqs. (6)–(11). The additional thin line in the eccentricity plot corresponds to e_{crit} —the critical value of eccentricity of a particle, such that the particle collides with Mars in the pericenter of the orbit. The thick grey solid line in the middle and bottom panels corresponds to averaged values of the eccentricity and inclination.

constant (Fig. 4, middle), whereas the inclination shows a gradual decrease of amplitude (Fig. 4, bottom). All these trends are stronger for smaller grains. The sudden

change in the dynamics of the 7.5 μm grain after about 21 000 M.y., which strongly attracts attention in Fig. 4, is discussed in detail in the next section.

3.5. Abrupt orbit modifications and chaos

In Fig. 5 we show dynamical evolution of different-sized Deimos ejecta under the influence of radiation pressure, Mars' oblateness, and the Poynting–Robertson drag over a long time span. Instead of analysing gradual changes of periods and amplitudes in e and i , we now focus on the evolution of the mean values of elements. Therefore, we plot time-average values of the orbital elements a_{mean} , e_{mean} , i_{mean} over adjacent time intervals of 500 M.y. Shown are orbital histories of particles with zero initial e and i of three sizes: 15 (thick solid), 10 (thick dashed), and 7.5 μm (thick dotted lines).

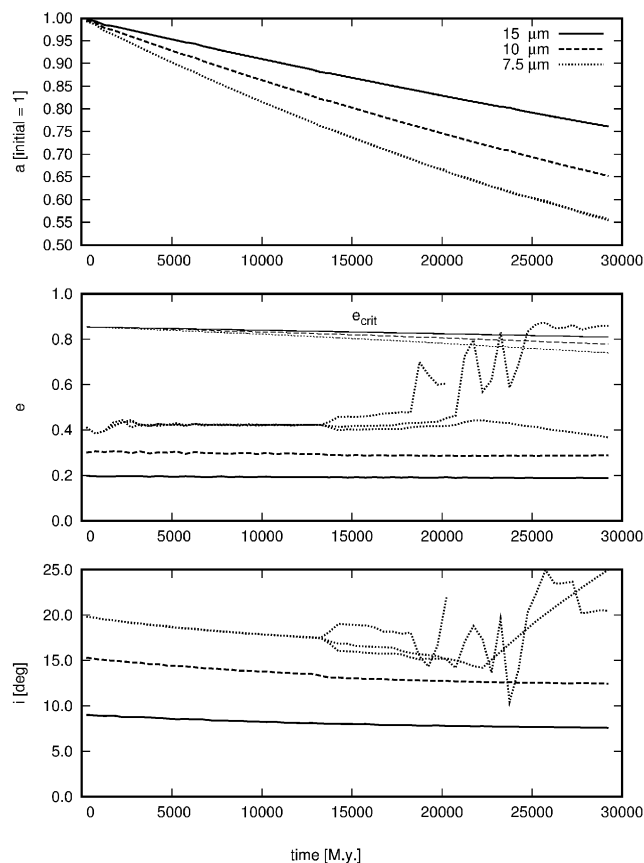


Fig. 5. Dynamical evolution of different-sized Deimos ejecta under the radiation pressure, Mars' oblateness and the PR drag over a long time span. From top to bottom: semimajor axes, eccentricities, and inclinations. The curves represent time-average values of the orbital elements over adjacent time intervals of 500 M.y. Shown are orbital histories of particles of three sizes: 15 (thick solid), 10 (thick dashed), and 7.5 μm (thick dotted lines). On the middle panel, we overplot the critical eccentricity for which the pericenter is at the planetary surface. Since it depends on the (size-dependent) value of the semimajor axis, we plot the critical eccentricity of the particles of a certain size with a thin line of the same style (solid, dashed, or dotted) as the one used to depict the orbital elements. For smallest radius, 7.5 μm , we launched 3 particles with slightly different initial values of the solar longitude: $\lambda_{\odot} = 180^{\circ}$, 181° , and 182° . At a certain instant of time, the three curves drastically diverge. This is a saddle separatrix chaos discussed in the text.

For the two larger sizes, we only see a nearly constant mean e (which is larger for smaller particles), and a gradually decreasing mean i (larger values and faster decrease for smaller particles). This is consistent with the analysis given in the previous section.

For smallest radius, 7.5 μm , however, sudden changes start to occur after $\approx 13\,000$ M.y. of their orbital evolution. We launched 3 particles with slightly different initial values of the solar longitude: $\lambda_{\odot} = 180^{\circ}$, 181° , and 182° . At a certain instant of time, three curves drastically diverge. An exact moment when it happens varies from one particle to another (see figure). The same effect would result from a change in *any* of the initial data, even by an *arbitrarily small* amount. All this is indicative for chaos, the appearance of which needs to be explained. Before we proceed with that analysis, we note that, after the particle has achieved the chaotic regime, the eccentricity reaches the critical value, and the grain is lost at the Martian surface. Particles smaller than 7.5 μm , but still above the critical radius, reveal the same behaviour (not shown in the figure). The smaller the grain, the sooner it lands in chaos.

To explain the phenomenon, it is useful to analyse phase portraits of the dynamical system. Krivov et al. (1996) and Hamilton and Krivov (1996) studied a simplified 2D problem (neglecting Mars' obliquity ε and setting inclination i to zero), which is integrable, allowing an exhaustive analytic treatment. As variables, they used eccentricity e and solar angle $\phi_{\odot} \equiv \tilde{\omega} - \lambda_{\odot}$. The latter variable measures the angle between the planetocentric directions toward orbit's pericenter and the Sun. They constructed phase portraits in the $e - \phi_{\odot}$ plane and investigated the location and properties of fixed points. Fig. 6 depicts such phase portraits for Deimos ejecta with the same sizes as in Fig. 5, found from numerical integrations of Eqs. (6)–(11). The orbits of larger, 15 and 10 μm grains (left) are close to circles surrounding a fixed point (local maximum, P_3 in the notation of Hamilton and Krivov (1996)) located on the $e \cos \phi_{\odot}$ axis (cf. Fig. 3 of Hamilton and Krivov (1996)). The trajectory of a smaller, 7.5 μm particle, reveals a more complicated structure, including the circle just described and an additional outer circle (right). A “bridge” between both circles is associated with another fixed point, a saddle P_4 , also located on the $e \cos \phi_{\odot}$ axis.

To explain the behaviour of the 7.5 μm -sized grain, we computed phase portraits in the simplified 2D problem analytically by means of the Hamilton and Krivov (1996) formulas. Fig. 7 plots a family of trajectories of 7.5 μm -sized Deimos grains starting from slightly different points around $e = 0$. Three panels correspond to different values of semimajor axis a/a_0 (1.0, 0.7, and 0.6) and therefore to different stages of the dynamical evolution. As semimajor axis decreases (C decreases, ω increases), P_3 migrates only slowly to the left, while the

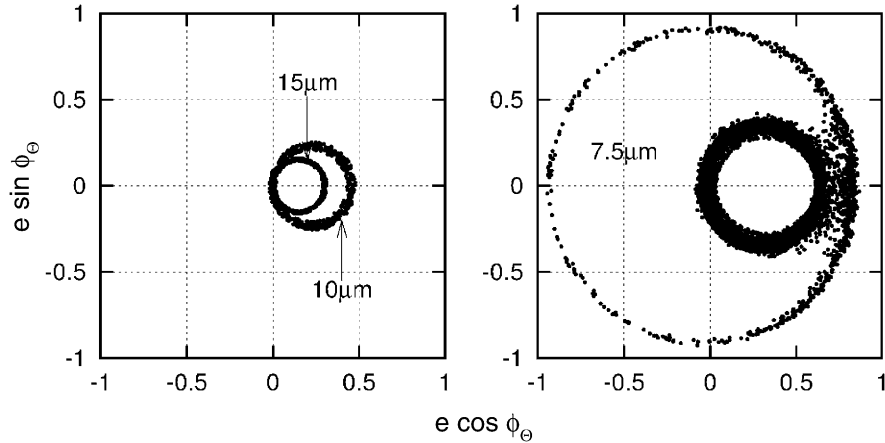


Fig. 6. Polar plot of eccentricity e versus solar angle $\phi_0 \equiv \tilde{\omega} - \lambda_\odot$ for Deimos particles with radii 15 and 10 μm (left) and 7.5 μm (right).

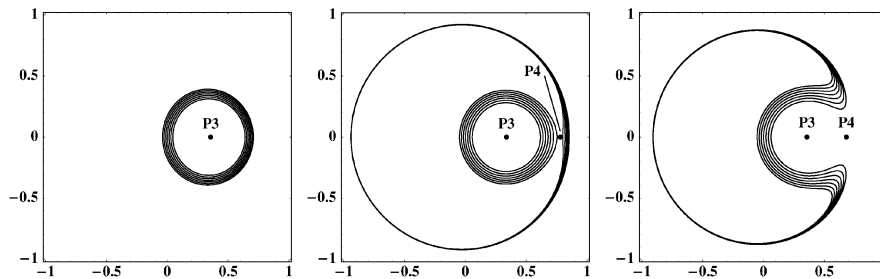


Fig. 7. A family of trajectories of 7.5 μm -sized Deimos grains starting with different initial eccentricities close to zero, calculated analytically from a simplified 2D problem. The axes are the same as in Fig. 6. Panels from left to right correspond to diminishing values of semimajor axis a/a_0 (1.0, 0.7, and 0.6) and therefore to different stages of the dynamical evolution. Cf. Fig. 6 (right).

saddle P_4 approaches from the right much faster. When $a/a_0 = 0.7$ ($P_3 = [0.34, 0]$ and $P_4 = [0.78, 0]$), the $e_0 = 0$ trajectory reaches the separatrix associated with saddle. As this happens, the trajectory flips from the libration regime (inner circle, solar angle librates about zero) to the circulation regime (outer circle, solar angle takes all values between 0° and 360°).

Thus, some of the trajectories with e_0 close to zero pass by the saddle from the left and follow inner circles. Others go to the right of P_4 and swerve to a large outer circle. Still, the integrable 2D system depicted in Fig. 7 does not contain any chaos: every trajectory belongs to one regime or another. However, adding the third dimension ($\varepsilon \neq 0$, $i \neq 0$ in Eqs. (6)–(11)) makes the system non-integrable and can cause unpredictable switches between both regimes along one and the same trajectory. The same effect can be triggered by small perturbations imposed on a trajectory. Thus the peculiar behaviour of smaller ejecta is a classical saddle separatrix chaos. A similar behaviour was identified earlier in the dynamics of the Phobos ejecta under radiation pressure and Mars' oblateness (without the PR effect), however at much larger grain sizes of

hundreds μm (Krivov et al., 1996; Hamilton and Krivov, 1996).

4. Lifetimes of particles in the Deimos torus

4.1. Impacts with Deimos and Phobos

The main loss mechanism for the Deimos ejecta is collision with the parent body, Deimos, as well as with the other satellite—Phobos. In Fig. 8 we show the evolution of pericentric and apocentric distances of different-sized Deimos grains. For the smallest size, 7.5 μm , the amplitude of the eccentricity oscillations is high enough for the grain to cross not only the Deimos orbit, but also the orbit of Phobos from the very beginning. Thus both moons act as sinks, efficiently removing the particles. The orbit of the medium-sized grain (11 μm) initially crosses only the Deimos orbit. In the course of the PR evolution, both pericentric and apocentric distances decrease until the apocentre crosses the Deimos orbit at $t \approx 26\,000$ M.y., stopping further re-accretion of the ejecta by this moon. However, at the

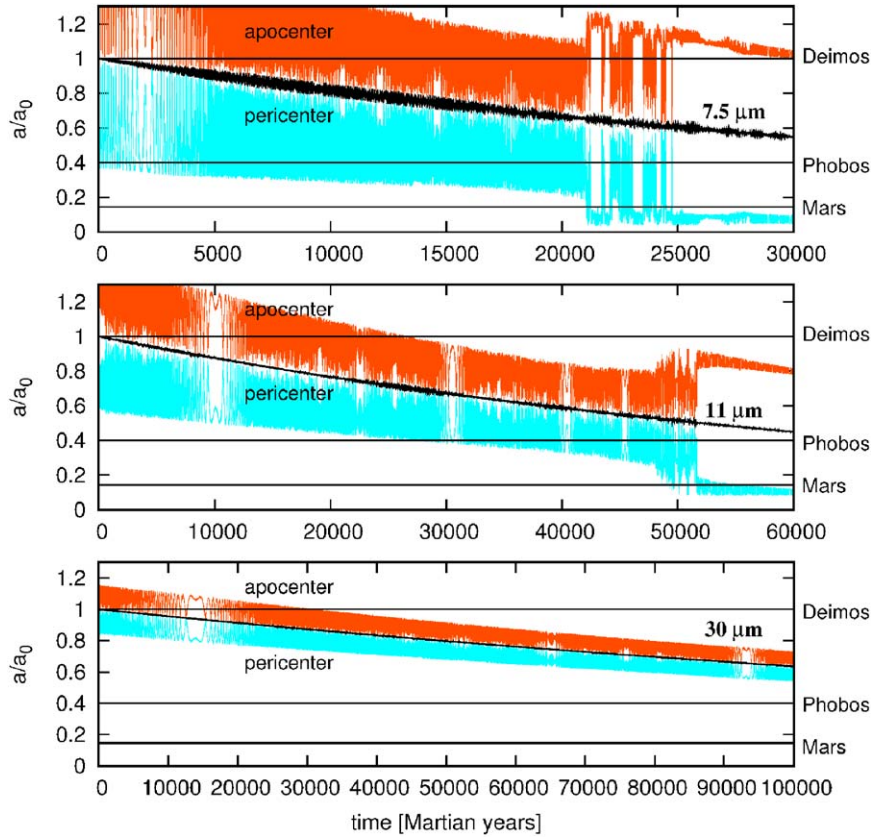


Fig. 8. Time evolution of instantaneous pericentric distance (light grey) and apocentric distance (dark grey) of Deimos particles with radii 7.5 μm (top), 11 μm (middle) and 30 μm (bottom). The distances are scaled to the semimajor axis of the Deimos orbit. Horizontal straight lines mark orbital radii of Deimos, Phobos and the surface of Mars.

same moment the pericentric distance shrinks to the size of the Phobos orbit; it is now Phobos that eliminates the particles. For larger particles, the latter event occurs later than the former. During some period of time, the whole orbit of a grain lies between the orbits of Phobos and Deimos, crossing neither of them. The larger the grain, the slower the PR evolution, the smaller the e_{max} and therefore the longer the time span when the particle safely orbits Mars between both satellites. Therefore, one would expect to find long-lived particles in this size regime.

To make quantitative estimates, we consider e -folding lifetimes against collisions with both moons—Phobos T_p and Deimos T_d ; each of them having an infinitely large value when the grain orbits do not intersect the orbit of the respective satellite. For each of the two moons, we can use Öpik’s (1976) formula

$$T_{\text{moon}} \approx \pi \sqrt{\sin^2 i + \sin^2 i_{\text{moon}}} \left(\frac{a_{\text{moon}}}{R_{\text{moon}}} \right)^2 \left(\frac{u}{u_r} \right) P, \quad (21)$$

where i is mean inclination of particle’s orbit, i_{moon} is that of moon’s orbit (both being measured from Mars’ equatorial plane); R_{moon} and a_{moon} are the satellite radius and semimajor axis of its orbit; u is the average

grain velocity relative to the moon; u_r is the radial component of u and P is the orbital period of the particles. Further,

$$u = \sqrt{3 - \frac{1}{A} - 2\sqrt{A(1 - e^2)} \cos i} \quad \text{and} \quad (22)$$

$$u_r = \sqrt{2 - \frac{1}{A} - A(1 - e^2)},$$

with $A \equiv a/a_{\text{moon}}$ being the dimensionless semimajor axis of the particle orbit. The ratio u/u_r weakly depends on the orbital elements, including eccentricity and, for $A \approx 1$ and small i , is of the order of unity (Hamilton and Burns, 1994; Krivov and Hamilton, 1997).

The collisional lifetimes were then calculated as follows. As before, we numerically integrated Eqs. (6)–(11) over a sufficiently long interval for a considered particle size. Instantaneous values of the orbital elements a , e , i were used in Eqs. (21)–(22) to compute separately $T_p(t)$ and $T_d(t)$. The collisional lifetime against collisions with both moons was then evaluated as $T_{\text{impact}}^{-1} = T_p^{-1} + T_d^{-1}$. Because orbital elements entering Eqs. (21) and (22) change with time, T_{impact} will be a function of time as well. Thus, $T_{\text{impact}}(t)$ has an “instantaneous” meaning: it is the lifetime one would

expect, if at the moment t the particle’s orbital elements $a(t)$, $e(t)$, $i(t)$ were “frozen”. For the same grain sizes, we then calculated the fraction f of surviving particles, as a function of time. This was done by simultaneously integrating, together with Eqs. (6)–(11), the differential equation

$$\frac{df(t)}{dt} = -T_{\text{impact}}^{-1}(t)f(t), \tag{23}$$

assuming $f(0) = 1$ as an initial condition. Fig. 9 depicts the results, which we can interpret with the aid of Fig. 8. Particles with radii below 11 μm are removed by both Deimos and Phobos, and so $f(t)$ decreases rapidly. Curves for larger particles contain flat portions, whose length increases with radius. Each “plateau” corresponds to a period when the entire orbit lies between the orbits of Deimos and Phobos. It drops when a particle becomes a Phobos-crosser.

With the function $f(t)$, it is easy to calculate a steady-state number of grains for each grain radius. Denoting by $N^+(s)$ the dust production rate from the Deimos surface in a unit size interval around s and assuming $N^+(s)$ to be constant in time, we have

$$N_{\text{ss}}(s) = N^+(s) \int_0^\infty f(s, t) dt, \tag{24}$$

where we have added s as an argument of f . The resulting curve for $N^+ \equiv 1$ (i.e. the integral in Eq. (24)) is plotted in Fig. 10, showing a strong maximum around $\approx 13 \mu\text{m}$. The position of the maximum results from a trade-off between two effects. On the one hand, starting from 11 μm , the duration of the “safe” stage of the particle evolution increases with its size. Accordingly, the “plateau” in Fig. 9 gets longer. On the other hand, a fraction of grains that are not removed by Deimos before they reach that stage decreases with radius—the level of the “plateau” in Fig. 9 gets smaller with particle’s size.

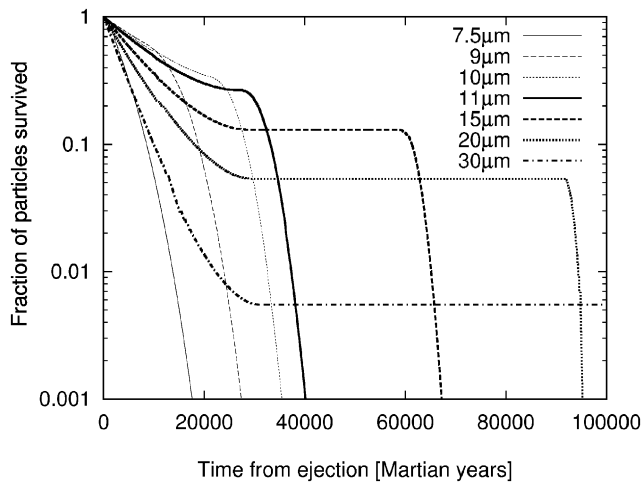


Fig. 9. Fraction of particles surviving collisions with Deimos and Phobos.

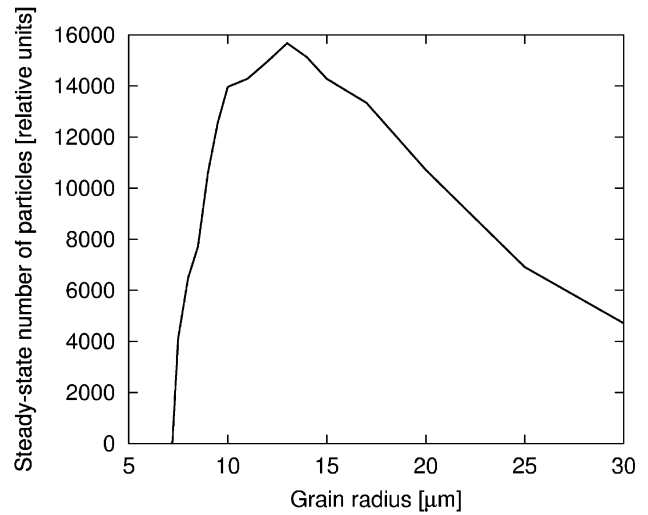


Fig. 10. Steady-state number of particles as a function of their size. The numbers are relative, assuming that the production rate per unit radius interval is the same for all radii. Absolute numbers can be obtained by multiplying the depicted function by the expected production rate as a function of size.

In reality, smaller particles must be produced at much higher rates than bigger ones, so that $N^+(s)$ is approximately a power law with the exponent close to -3.5 (Krivov and Hamilton, 1997). Multiplication of the integral by this distribution would give even sharper peak at nearly the same size. Thus, particles with $s \approx 10\text{--}15 \mu\text{m}$ are expected to dominate the number density of the Deimos torus. One can show that they will dominate the cross section of dust in the torus as well. These particles, “hanging” in the region between the orbits of Deimos and Phobos, are large enough to pose serious threat for a spacecraft; see Section 4.2 for estimates. This should be kept in mind in space mission planning.

Note that N^+ is a dimensional quantity; in plotting N_{ss} in Fig. 10, we have set $N^+ = 1 \text{ M.y.}^{-1}$. Therefore, the same curve can also be interpreted as a mean lifetime of different-sized particles in Martian years. The maximum corresponds to $\approx 16\,000 \text{ M.y.}$ This mean lifetime is not to be mixed with the maximum possible lifetime of the grains. Fig. 9 shows, for instance, that about 13% of 15 μm -sized grains stay in orbits for $\approx 6 \times 10^4 \text{ M.y.}$ and 5% of 20 μm -sized particles are lost only after $\approx 1 \times 10^5 \text{ M.y.}$

4.2. Mutual collisions

We now look at possible loss mechanisms of grains other than impacts with Mars and its two moons. Sublimation and sputtering could be efficient for pure icy particles (Leinert and Grün, 1990), but are not important for the regolith grains. Lifetimes of 10 μm -sized particles against collisions with interplanetary grains are of the order of 10^6 M.y. (Grün et al., 1985).

The only potentially important additional sink is mutual collisions of the torus particles.

As grains with $s \sim 10\text{--}15\ \mu\text{m}$ have much larger number densities in the Deimos torus than the others, these grains have the shortest collisional lifetime, and the latter is largely determined by their collisions with themselves. Thus, for the sake of simple estimates, we consider a “partial” Deimos torus, composed solely by particles in the size range $10\ \mu\text{m} \leq s \leq 15\ \mu\text{m}$. The lifetime against mutual collisions is

$$T_{\text{coll}} \approx (n\sigma v_{\text{imp}})^{-1}. \quad (25)$$

Here, n is the number density of the particles, $v_{\text{imp}} \approx v_0 \sqrt{e_{\text{mean}}^2 + i_{\text{mean}}^2}$ the mean relative velocity between them (v_0 is the Deimos orbital velocity), and $\sigma = 2\pi s^2$ the collisional cross section. The number density is approximately given by

$$n \approx N^+ T / V, \quad (26)$$

where now N^+ is the production rate of $10\text{--}15\ \mu\text{m}$ dust from the surface, T is the mean lifetime against both impacts with the moons and grain–grain collisions, and V is the torus volume:

$$V \approx 8\pi a_0^3 e_{\text{max}} i_{\text{max}}, \quad (27)$$

with a_0 being the radius of the Deimos orbit, e_{max} and i_{max} typical amplitudes of oscillations of eccentricity and inclination. Eqs. (25)–(27) yield

$$T_{\text{coll}} \approx \frac{8\pi a_0^3 e_{\text{max}} i_{\text{max}}}{N^+ T \sigma v_{\text{imp}}}. \quad (28)$$

Taking into account an obvious relation $T^{-1} = T_{\text{impact}}^{-1} + T_{\text{coll}}^{-1}$, we find

$$\frac{1}{T} \approx \frac{1}{T_{\text{impact}}} + \frac{N^+ T \sigma v_{\text{imp}}}{8\pi a_0^3 e_{\text{max}} i_{\text{max}}}. \quad (29)$$

All quantities in Eq. (29) except for N^+ are determined by the dynamics. From the results of previous sections for $s \approx 10\ \mu\text{m}$, we take $e_{\text{mean}} \approx i_{\text{mean}} \approx 0.3\ \text{rad}$ (Figs. 4–5) to get $v_{\text{imp}} \approx 0.8\ \text{km s}^{-1}$, $e_{\text{max}} \approx i_{\text{max}} \approx 0.4\ \text{rad}$, and $T_{\text{impact}} \approx 15\,000\ \text{M.y.}$ (Fig. 10). In contrast, N^+ is determined by the dust production mechanism from the satellite surface. Previous estimates (see e.g. Krivov and Hamilton, 1997) gave values $N^+ \sim 10^{6\pm 1}\ \text{s}^{-1}$ for $10\ \mu\text{m} \leq s \leq 15\ \mu\text{m}$.

For any value of N^+ , Eq. (29) can be solved for T , and accordingly T_{coll} can be found from Eq. (28). We can also estimate the geometrical edge-on optical depth of the torus (Krivov and Hamilton, 1997)

$$\tau_{\parallel} \approx \frac{N^+ T \sigma v_{\text{imp}}}{8a_0^2 i_{\text{max}}}. \quad (30)$$

For a lower dust production rate $N^+ = 10^5\ \text{s}^{-1}$, mutual collisions are less important than impacts with the moons: we find $T_{\text{coll}} = 30\,000\ \text{M.y.}$, which is larger than

$T_{\text{impact}} = 15\,000\ \text{M.y.}$ The “combined” lifetime is $T = 10\,000\ \text{M.y.}$, and $\tau_{\parallel} \approx 2 \times 10^{-8}$. However, for a higher dust production rate $N^+ = 10^7\ \text{s}^{-1}$, T_{coll} is much shorter than T_{impact} : $T_{\text{coll}} = 1900\ \text{M.y.}$ In this case, $T = 1600\ \text{M.y.}$, and $\tau_{\parallel} \approx 4 \times 10^{-7}$. Actual optical depth should be somewhat higher, due to contributions made by particles $s > 15\ \mu\text{m}$. Still, the expected optical depth is below the current observational limit $\tau_{\parallel} < 10^{-6}$ (Shoemaker et al., 2001).

It is easy to estimate a meteoric hazard for a spacecraft. Assume it to orbit Mars within the Deimos torus. The dust flux, i.e. the number of impacts per unit area per unit time, is simply $n v_{\text{imp}}$. For $N^+ = 10^5\text{--}10^7\ \text{s}^{-1}$, one should expect $10^2\text{--}10^3$ impacts of $10\ \mu\text{m}$ -sized grains per $1\ \text{m}^2$ during one orbital revolution around Mars.

We finally make one concluding remark. The dynamical effects considered in Section 3 are only possible because for particles with radii somewhat above s_{crit} the lifetime against accretion by Deimos is comparable to the PR drift time. We have just found that the lifetime against mutual collisions is of the same order of magnitude, too! All this is a pure coincidence: were the size of the Deimos and Phobos orbits, or the size of Deimos itself, different from the actual values, that would no longer be true.

5. Structure of the Deimos torus

The same numerical integrations were used to construct snapshots of the Deimos torus. To this end, we simply converted instantaneous values of the osculating elements, complemented with a random value of the mean anomaly, into Cartesian coordinates.

The results are depicted in Fig. 11. It shows snapshots of the torus of $11\ \mu\text{m}$ grains at two different time epochs: for ‘young’ particles soon after ejection (left panels) and for ‘old’ particles after $3 \times 10^4\ \text{M.y.}$ of the orbital evolution (right panels). In each case, the torus is shown in three different projections. All snapshots are constructed for one and the same Martian season (autumn equinox, $\lambda_{\odot} = 180^\circ$).

We see that long-term influence of perturbing forces results in a gradual change of the torus geometry with time. The following effects take place:

- (1) A gradual contraction of the torus (Figs. 11a–c versus d–f);
- (2) decrease of the torus displacement and azimuthal symmetrisation of the torus (Figs. 11a–b versus d–e);
- (3) flattening of the torus (Figs. 11b–c versus e–f);
- (4) decrease of the torus tilt (Fig. 11c versus f).

In the same figure, we overplot the snapshots of the Phobos torus of like-sized, $11\ \mu\text{m}$ -particles. Both tori start to progressively overlap and the particles of Phobos

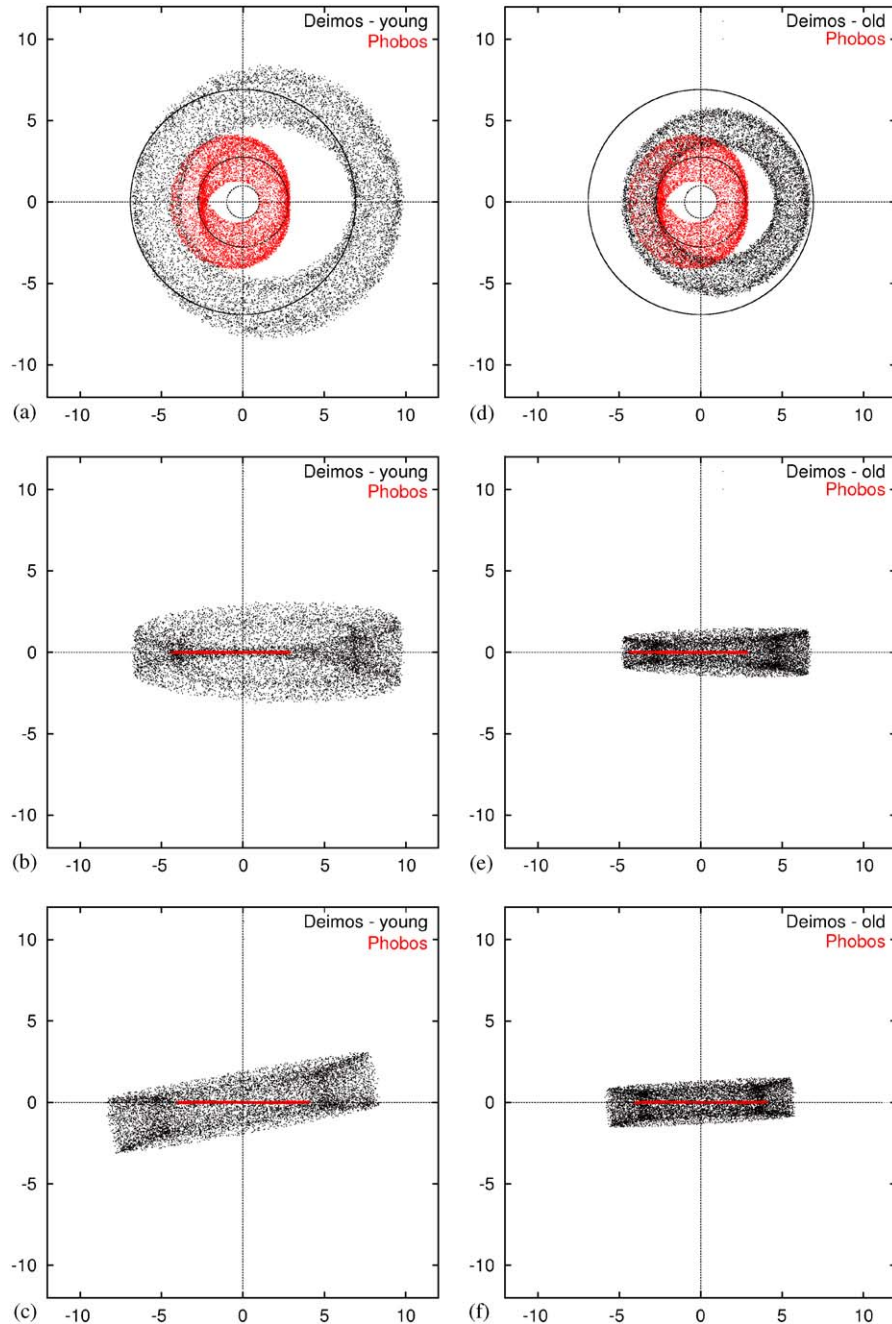


Fig. 11. Snapshots of the Deimos torus formed by $11\ \mu\text{m}$ particles under the influence of the J2, RP and PR forces. Left: ‘young’ particles in the beginning of evolution; right: ‘old’ particles after 3×10^4 M.y. Top to bottom: XY , XZ , YZ projections of the equatorial equinoctial coordinate system centred on Mars. All snapshots are given for the Martian autumn equinox (the Sun is on the negative OX axis). Coordinates are in the units of Mars’ radii R_M . The Phobos torus of like-sized particles is overplotted on all panels (inner thin ring-like configuration). In the upper panels, small inner circle represents Mars and two outer circles are the orbits of Phobos and Deimos.

and Deimos increasingly mix. After 50 000 M.y. (not shown in the figure), the azimuthal projections of both tori would become nearly indistinguishable. Still, the Deimos torus remains much thicker than the Phobos one, which is easy to explain. Although evolved Deimos particles acquire semimajor axes and eccentricities close to those of Phobos grains, the Deimos particles arrive at the “Phobos regime” with larger orbital inclinations of

$\sim 10^\circ$ (see Fig. 4) than the Phobos grains have. In this sense, even in the “Phobos regime”, the Deimos ejecta “remember” their dynamical history.

The scatter plots shown in each column of Fig. 11 represent instantaneous configuration of dust ejected at the same instant of time, 0 M.y. or 30 000 M.y. ago. They can be interpreted as a real configuration produced by an individual impact of a large meteorite onto the

Deimos surface. A “steady-state” Deimos torus sustained by a continuous flux of micrometeorites consists of particles that were injected into the system at different moments of time in the past. Therefore, snapshots like those depicted in Fig. 11 should be summed up with weights proportional to the absolute numbers of particles remaining in the system at the moment of observation. As the population of particles ejected simultaneously will be decaying with time, “older” populations will get lower weights than “younger” ones. We argue, however, that the resulting steady-state torus will bear clear signatures of the PR dynamics, being smaller in size, more symmetric, and more aligned to the equatorial plane than the “classical” torus predicted in earlier studies and shown in the left panels of Fig. 11.

6. Conclusions

In this paper, we have considered dynamics of dusty ejecta from Deimos under the combined action of three perturbing forces: solar RP, Mars’ J2, and the PR force. Inclusion of the latter force into the model is new and is justified by long lifetimes of the Deimos grains, up to $\sim 10^5$ years. We have also provided better estimates of the lifetimes of different-sized Deimos ejecta and analysed spatial structure of the presumed Deimos torus. Our main conclusions are as follows:

1. The PR decay of the semimajor axes does not affect the oscillations of the orbital eccentricity, but causes an adiabatic decrease of amplitudes and periods of oscillations in orbital inclinations predicted in the framework of the underlying RP+J2 problem.

2. Smallest of the long-lived Deimos grains (radius $\approx 5\text{--}10\ \mu\text{m}$) may reach a chaotic regime, resulting in unpredictable and abrupt changes of their dynamics. Chaos is associated with the motion in the vicinity of a saddle separatrix of the underlying dynamical system.

3. The particles just above that size ($\approx 10\text{--}15\ \mu\text{m}$) are expected to dominate the Deimos torus. Impacts with both martian moons and mutual collisions can be equally important in limiting the lifetimes of these particles. Their PR drift and gradual changes in the dynamics should be reflected by the torus structure. In addition to a population, appreciably inclined and shifted towards the Sun, the torus should contain a more contracted, less asymmetric, and less tilted component interior to the orbit of Deimos.

Acknowledgements

We thank Antal Juhász and an anonymous referee for useful and speedy reviews of this work. We are

grateful to Miodrag Sremčević for sharing with us his skills in using the IDL and Mathematica[®] packages. Helpful discussions with James E. Howard are appreciated. This research was funded by Deutsche Forschungsgemeinschaft (DFG), project KR 2164/1-1. Part of the work was also supported by Deutsches Zentrum für Luft- und Raumfahrt (DLR), project 50 OH 0003.

References

- Burns, J.A., Lamy, P.L., Soter, S., 1979. Radiation forces on small particles in the Solar System. *Icarus* 40, 1–48.
- Everhart, E., 1985. An efficient integrator that uses Gauss-Radau spacing. In: Carusi, A., Valsecchi, G.B. (Eds.), *Dynamics of Comets: their Origin and Evolution*. Dordrecht, Reidel, pp. 185–202.
- Grün, E., Zook, H.A., Fechtig, H., Giese, R.H., 1985. Collisional balance of the meteoritic complex. *Icarus* 62, 244–272.
- Hamilton, D.P., 1996. The asymmetric time-variable rings of Mars. *Icarus* 119, 153–172.
- Hamilton, D.P., Burns, J.A., 1994. Origin of Saturn’s E ring: self-sustained, naturally. *Science* 264, 550–553.
- Hamilton, D.P., Krivov, A.V., 1996. Circumplanetary dust dynamics: effects of solar gravity, radiation pressure, planetary oblateness, and electromagnetism. *Icarus* 123, 503–523.
- Horányi, M., Burns, J.A., Tétrallyay, M., Luhmann, J.G., 1990. Toward understanding the fate of dust lost from the Martian satellites. *Geophys. Res. Lett.* 17, 853–856.
- Horányi, M., Tétrallyay, M., Juhász, A., Luhmann, J.G., 1991. The dynamics of submicron-sized dust particles lost from Phobos. *J. Geophys. Res.* 96, 11,283–11,290.
- Howard, J.E., Krivov, A.V., Spahn, F., 2003. Transverse halo orbits about Mars? *Geophys. Res. Lett.* 30, No. 13.
- Ishimoto, H., 1996. Formation of Phobos/Deimos dust rings. *Icarus* 122, 153–165.
- Juhász, A., Horányi, M., 1995. Dust torus around Mars. *J. Geophys. Res.* 100, 3277–3284.
- Kholshchevnikov, K.V., Krivov, A.V., Sokolov, L.L., Titov, V.B., 1993. The dust torus around Phobos orbit. *Icarus* 105, 351–362.
- Kimura, H., Ishimoto, H., Mukai, T., 1997. A study on solar dust ring formation based on fractal dust models. *Astron. Astrophys.* 326, 263–270.
- Krivov, A.V., 1996. On the dust belts of Mars. *Astron. Astrophys.* 291, 657–663.
- Krivov, A.V., Hamilton, D.P., 1997. Martian dust belts: waiting for discovery. *Icarus* 128, 335–353.
- Krivov, A.V., Sokolov, L.L., Dikarev, V.V., 1996. Dynamics of Mars-orbiting dust: effects of light pressure and planetary oblateness. *Celestial Mechanics Dynamical Astron.* 63, 313–339.
- Krivov, A.V., Kimura, H., Mann, I., 1998. Dynamics of dust near the Sun. *Icarus* 134, 311–327.
- Leinert, C., Grün, E., 1990. Interplanetary dust. In: Schwenn, R., Marsch, E. (Eds.), *Physics of the Inner Heliosphere. I. Large-Scale Phenomena*. Springer, Berlin, pp. 207–275.
- Öpik, E.J., 1976. *Interplanetary Encounters: Close Range Gravitational Interactions*. Elsevier, New York.
- Showalter, M.R., Hamilton, D.P., Nicholson, P.D., 2001. A search for martian dust rings. *Bull. Am. Astron. Soc.* 33, 1095.
- Soter, S., 1971. The dust belts of Mars. Report of Center for Radiophysics and Space Research, vol. 462.